

Modes of covariability between sea surface temperature and wind stress intraseasonal anomalies along the coast of Peru from satellite observations (2000–2008)

B. Dewitte,^{1,2,3} S. Illig,¹ L. Renault,⁴ K. Goubanova,^{1,2,3} K. Takahashi,² D. Gushchina,⁵ K. Mosquera,^{2,6} and S. Purca³

Received 29 June 2010; revised 24 January 2011; accepted 9 February 2011; published 29 April 2011.

[1] The Tropical Rainfall Measuring Mission Microwave Imager sea surface temperature (SST) and QuikSCAT wind stress satellite data are used to investigate the intraseasonal upwelling variability along the coast of Peru over the period 2000–2008. Two regions of peak variance correspond to the central Peru region (Pisco region, 15°S) and the northern Peru region (Piura region, 5°S). A covariance analysis reveals a significant coherency between winds and SST anomalies off Pisco, consistent with Ekman pumping and transport dynamics. The upwelling cell consists in a meridionally extended fringe of colder (warmer) water extending as far as 250 km from the coast at 15°S. In the Piura region, the intraseasonal covariability pattern is represented by two modes, one relevant to the direct Ekman dynamics and the other one associated with the remote forcing of intraseasonal oceanic Kelvin wave. Two regimes of variability are evidenced. A low-period regime (10–25 days) is the signature of Ekman transport/pumping dynamics and is remotely forced by the migratory atmospheric disturbances across the southeastern Pacific anticyclone. A high-period regime (35–60 day band) is associated with the combined forcing of oceanic equatorial Kelvin waves and migratory atmospheric disturbances in the midlatitudes. In particular, the modes of covariability exhibit a prominent ~50 day period energy peak. It is shown that this period arises from the impact of the first two baroclinic modes Kelvin wave, with the second baroclinic mode Kelvin wave being more influential on the Piura region.

Citation: Dewitte, B., S. Illig, L. Renault, K. Goubanova, K. Takahashi, D. Gushchina, K. Mosquera, and S. Purca (2011), Modes of covariability between sea surface temperature and wind stress intraseasonal anomalies along the coast of Peru from satellite observations (2000–2008), *J. Geophys. Res.*, 116, C04028, doi:10.1029/2010JC006495.

1. Introduction

[2] The west coast of South America hosts a very productive oceanic ecosystem [Carr, 2001]. From a physical perspective, this is due to the upwelling favorable conditions along the coast resulting from the southeast Pacific (SEP) anticyclone in the subtropical latitudes that drives an alongshore northward surface flow along the coast from 40°S to the equator. Whereas off central Chile, these alongshore winds are intense because of the close location of the center of the SEP anticyclone, off Peru they tend to weaken as they feed the southeast branch of the equatorial

trade winds. Despite these weaker alongshore circulation, the upwelling can be as intense as off Chile due to the proximity to the equator making Ekman pumping and transport more effective [Ekman, 1905]. Interestingly, the Peru ecosystem is also more productive than its Chilean counterpart. The reasons for this remain unclear. Whereas biogeochemical conditions may be a key parameter for explaining such feature, the peculiarities of the environmental forcing is certainly a factor that comes into play. Two main aspects of the environmental forcing are to be considered (1) the equatorial Kelvin wave that is highly connected to the coastal variability and (2) the local wind forcing that controls the upwelling variability through Ekman pumping and transport. Both involve a broad spectrum of timescales, ranging from daily to interannual time-scales. For instance, in the period range from days to weeks, sea level and subsurface temperature variability has been found to be associated mainly with coastal Kelvin waves [Smith, 1978; Cornejo-Rodriguez and Enfield, 1987], mainly during winter time [Cornejo-Rodriguez and Enfield, 1987]. On periods longer than 2 weeks, the dominant remote wave forcing is associated with equatorial Kelvin waves, whereas

¹Laboratoire d'Etudes en Géophysique et Océanographie Spatiale, Toulouse, France.

²Instituto Geofísico del Peru, Lima, Peru.

³Instituto del Mar del Peru, Callao, Peru.

⁴Mediterranean Institute for Advanced Studies, Esporles, Spain.

⁵Faculty of Geography, Moscow State University, Moscow, Russia.

⁶Also at Laboratoire d'Etudes en Géophysique et Océanographie Spatiale, Toulouse, France.

on shorter timescales mixed Rossby-gravity waves appear to be more important [Enfield *et al.*, 1987]. On the other hand, measurements at 15°S (near Pisco) also indicate a significant role of wind forcing [Brink *et al.*, 1978; Stuart, 1981]. Other studies have been focused on the seasonal to interannual variability of the alongshore winds off Peru and their impact on upwelling rate [Enfield, 1981; Bakun, 1990; Halpern, 2002; Croquette *et al.*, 2007; Bakun and Weeks, 2008].

[3] The objectives of this paper is to examine the intraseasonal variability of sea surface temperature (SST) and wind stress derived from satellite data along the coast of Peru and identify seasonal modulation patterns. The main motivations for examining SST and wind stress are as follows:

[4] 1. Despite the fact that wind variability off central Peru shares many common features with the so-called Coastal Jet pattern off central Chile [Muñoz and Garreaud, 2005; Garreaud and Muñoz, 2005; Renault *et al.*, 2009], its dynamics remains unclear. Like for the central Chile coastal jet, at regional scale (~200–300 km), it is likely to be related to the migratory anticyclone at the midlatitudes [Renault *et al.*, 2009] and could therefore be considered as external forcing to the upwelling system. Local air-sea interaction, however, could be important for the wind, as has been found for the interannual timescales or longer [Enfield, 1981; Bakun, 1990].

[5] 2. There are a number of processes by which along-shore wind stress variability at intraseasonal timescales may impact mean upwelling conditions. For instance, intraseasonal variability of the winds may produce mixing reducing the effect of Ekman pumping on SST by increasing the mixed layer depth. They may also contribute to cool the waters through entrainment and vertical eddy heat flux at the bottom of the mixed layer. After upwelling favorable wind events, during periods where winds drop and temperature increases near-surface frontal processes lead to a restratification tendency that is thought to be significant [Fox-Kemper *et al.*, 2008; Fox-Kemper and Ferrari, 2008]. Renault *et al.* [2009] estimated the impact of the restratification process for an episode of coastal Jet event off central Chile and showed that it has a significant contribution on the rate of SST change. Due to the asymmetry (nonlinear character) of the mixing processes, it can result in a cumulative effect on the mean seasonal upwelling conditions [Bograd *et al.*, 2009]. Before documenting such processes from oceanographic data and/or model simulations, it is worth documenting the characteristics of the intraseasonal variability of wind stress and its impact on SST.

[6] 3. The oceanographic conditions off Peru are influenced by remote equatorial variability through the propagation of coastal-trapped Kelvin waves (cf. Colas *et al.* [2008] for the 1997–1998 El Niño). At intraseasonal timescales, the equatorial Kelvin wave is easily trapped along the coast [Clarke and Shi, 1991]. Its variability range from a few days to a few months and has a low-frequency modulation [Dewitte *et al.*, 2008]. The associated coastal trapped Kelvin wave can impact the coastal SST through mean vertical advection of anomalous temperature resulting in upwelling variability [Gutierrez *et al.*, 2008]. Such process is in essence different from upwelling variability associated with Ekman pumping. At intraseasonal timescales, it is not clear, however, which process dominates and at which timescale of variability. Along the coast of Chile, both local

and remote forcing appear to be important [Hormazábal *et al.*, 2001], but this is not yet clear for the Peruvian coast. This has implication for the understanding of the air-sea interactions in this region and also for prediction. In particular, since the intraseasonal equatorial Kelvin waves are generated in the western to central Pacific [Hendon *et al.*, 1999; Kessler and Kleeman, 2000; Roundy and Kiladis, 2006] and that it takes 2–3 months for them to reach the Peru coast, their impact on coastal upwelling can be anticipated more in advance than an episode of upwelling favorable winds associated with synoptic atmospheric conditions.

[7] The study focuses on the period 2000–2008. Beside the availability of the QuikSCAT wind data, this period is characterized by relatively weak interannual SST variability in the eastern tropical Pacific as compared to the previous decade that experienced the intense 1997–1998 El Niño. El Niño events over 2000–2008 have developed in the central Pacific [Yeh *et al.*, 2009] with a weaker amplitude than the one that develop in the eastern equatorial Pacific. In that sense, intraseasonal variability is emphasized, which also motivates the present study. Note that due to the rather coarse resolution of the QuikSCAT winds (with respect to the average Rossby radius of deformation in the latitude range of Peru) and the presence of a coastal blind zone for the satellite, our study also questions to which extent satellite data such the QuikSCAT product can be useful for documenting wind variability off the coast of Peru and associated upwelling variability.

[8] The paper is organized as follows: Section 2 presents the data sets and the methods. Section 3 provides a detailed description of the air-sea coupled modes of variability in the Pisco and Piura regions, whereas section 4 documents the relationship between regional modes of variability and the synoptic large-scale variability (oceanic and atmospheric). Section 5 is a discussion followed by concluding remarks.

2. Data Sets and Method

2.1. Data

2.1.1. Wind Stress From QuikSCAT

[9] The QuikSCAT satellite zonal and meridional wind stress on a $0.5^\circ \times 0.5^\circ$ latitude-longitude grid were obtained from Centre ERS d'Archivage et de Traitement (CERSAT) (<http://www.ifremer.fr/cersat/en/index.htm> [Centre ERS d'Archivage et de Traitement, 2002]). This product is built from both ascending and descending passes from discrete observations (available in JPL/PO.DAAC Level 2B product) over each day. There is no data for grid points located within 25 km of the coastline (satellite blind zone).

2.1.2. TMI Sea Surface Temperature

[10] Estimates of SST were obtained from the Tropical Rainfall Measuring Mission Microwave Imager (TMI) data set produced by Remote Sensing Systems (RSS, <http://www.remss.com/>). RSS provides daily 3 day averaged gridded SST on a regular $0.25^\circ \times 0.25^\circ$ latitude-longitude grid for latitudes lower than 38° . The TMI blind zone is within 50 km of the coast. It was noted, however, that some pixels near the coast could have unrealistic warm temperature, which we attribute to land contamination. It is believed that this does not impact the results presented here considering the rather broad cross-shore scale of the SST patterns that are described in this paper (which is of the order of 150–200 km). The SST estimates are

based mainly on emissions at 10.7 GHz, and are also largely uninfluenced by cloud cover, rain, aerosols and atmospheric water vapor [Wentz *et al.*, 2000]. However, the microwave retrievals are sensitive to (wind induced) sea surface roughness and this potential systematic error is a limitation of the present study. TMI comparisons with buoys give an RMS difference of about 0.6°K [Wentz *et al.*, 2000] due to a combination of instrumental (buoy) collocation error [Gentemann *et al.*, 2003]. Comparisons of the TMI SST estimates with buoy-measured near-surface ocean temperature show that, on greater than weekly timescales, TMI SST reproduces the characteristics of the 1 m buoy-observed temperatures in the tropical Pacific [Chelton *et al.*, 2001].

2.1.3. NCEP/NCAR Reanalysis

[11] The large-scale atmospheric conditions over the southeastern Pacific is diagnosed from the daily sea level pressure (SLP) and surface winds (U10m, V10m) from the National Centers for Environmental Prediction (NCEP)/National Center for Atmospheric Research (NCAR) reanalysis [Kalnay *et al.*, 1996]. The horizontal resolution of the data is $2.5^\circ \times 2.5^\circ$. The Reanalysis winds at 850 hPa were also used to calculate a Madden–Julian Oscillation [Madden and Julian, 1994] index (hereafter MJO) following the method by Wheeler and Kiladis [1999]. The method is based on a two-dimensional space-time Fourier analysis of the U850 anomalies field at each latitudes within the tropical belt (15°S – 15°N), then retaining eastward wave numbers 1–5 for periods of 30–95 days of the spectrum to recompose the signal through inverse space-time Fourier transform. To derive the MJO index, the MJO-filtered variability of the U850 field is averaged over the western Pacific region (5°S – 5°N ; 120°E – 180°E), where the peak activity is observed. This method has been used for MJO impact studies [Wheeler and Hendon, 2004; Hendon *et al.*, 2007] and process and model validation studies [McPhaden *et al.*, 2006; Lin *et al.*, 2006; Gushchina *et al.*, 2010].

2.1.4. Mercator

[12] The outputs of a global Ocean General Circulation Model (OGCM), named Mercator (http://www.mercator-ocean.fr/html/produits/index_en.html), are used to derive the amplitude of oceanic Kelvin contribution to sea level anomalies (AKm). Mercator is an eddy-permitting $1/4^\circ$ model, based on the primitive equations global general ocean circulation model OPA, written by Madec *et al.* [1998] and developed at the LOCEAN (CNRS/IRD laboratory). The model was forced with daily surface atmospheric conditions given by the ECMWF (European Center for Medium Range Weather Forecast) IFS (Integrated Forecast System) analysis. The simulation is hereafter referred to as Mercator (see Garric *et al.* [2008] for more details). Despite the fact that there is no assimilation of data in this experiment, the model has been shown to be skillful in capturing most aspects of the equatorial variability in the Pacific Ocean over the period 1992–2000 [Dewitte *et al.*, 2007; Illig *et al.*, 2007; Ramos *et al.*, 2008]. Here the experiment started the 4 April 1998 with prescribed conditions from climatological temperature and salinity. For the 2000–2008 period, the average correlation (rms difference) along the equator between sea level anomalies (relative to the mean seasonal cycle) as derived from satellite altimetry and model reaches 0.84 (3.21 cm). Comparison of model vertical zonal current (anomalies) and ADCP measurements from the TAO project (<http://www.pmel.noaa.gov/tao>) indicates

that the model realistically simulate the equatorial dynamics. For instance the average correlation between model and observation for between 30m and 210m of the four TAO moorings (165°E , 170°W ; 140°W and 110°W) reaches 0.60.

[13] To derive the Kelvin wave amplitude for the most energetic baroclinic modes ($m = 1, 2$), similar methodology to that described by Dewitte *et al.* [1999, 2003] is used. It consists in projecting the variability on the vertical (baroclinic) and horizontal (Kelvin and Rossby) modes as obtained from the vertical mode decomposition of the mean stratification over 2000–2008. This method was showed to be efficient in capturing the salient feature of the propagating characteristics and amplitude of the intraseasonal Kelvin wave in OGCM simulations (see an application for the SODA Reanalysis [Carton and Giese, 2008] by Dewitte *et al.* [2008] for instance). Intraseasonal anomalies are calculated in the same way than for the SST and QuikSCAT data (see below).

2.2. Method

[14] To extract the characteristics of the coupling between wind stress and SST anomalies, singular value decomposition (SVD) analysis [Bretherton *et al.*, 1992] was used. The SVD technique allows capturing the time/space modes that maximize the covariance between two data sets. In that sense, it is similar to an empirical orthogonal function (EOF) (which is based on the covariance matrix of a single field), but for each modes, one obtains two time series that, if they are highly correlated, might indicate a physically coupled mode. Considering SST ($sst(x, y, t)$) and both component of the wind stress ($txy(x, y, m, t)$, $m = 1, 2$ for zonal and meridional wind stress) anomalies, the method leads to the following decomposition:

$$sst(x, y, t) = \sum_{n=1}^N sst_n(x, y) \cdot f_n(t) \quad \text{and}$$

$$txy(x, y, m, t) = \sum_{n=1}^N txy_n(x, y, m) \cdot g_n(t),$$

where $sst_n(x, y)$ and $txy_n(x, y, m)$ are the mode patterns (eigenvectors) and $f_n(t)$ and $g_n(t)$ the associated time series (Principal Components). Those are obtained from the diagonalization of the covariance matrix formed from both fields. The coefficients of the diagonal matrix are the eigen values, generally called squared covariance fraction, and are ranked in the usual order from largest to smallest. They represent the squared covariance accounted for by each pair of eigen vectors. The eigenvectors provide the mode patterns for each field that are associated with the maximum covariance. See Bretherton *et al.* [1992] for more details on the method and to Wallace *et al.* [1992] for another application to geophysical fields. The method is also described in details by Renault *et al.* [2009] for a similar application.

[15] Intraseasonal anomalies are calculated following Lin *et al.* [2000]. It consists in first calculating the monthly means of the daily time series and then interpolating them back to a daily temporal grid using spline functions. The result is then retrieved from the original time series to derive daily intraseasonal anomalies. It was verified that this method is similar to an high-pass filter with a transfer function, estimated by computing intraseasonal anomalies

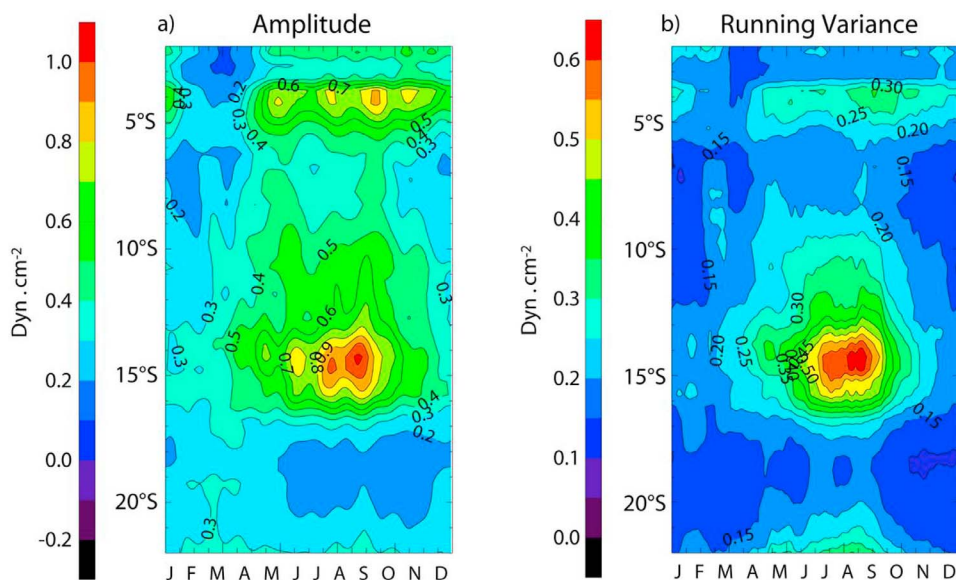


Figure 1. Climatological (a) amplitude and (b) 30 day running variance of the alongshore (equatorward) wind stress as derived from QuikSCAT over 2000–2008. Units are dyn cm^{-2} . Alongshore wind stress were obtained by projecting the meridional and zonal components on the direction of the coastline as derived from ETOPO (1° resolution) for 3° width segments.

of a daily Gaussian white noise, characterized by a -1 , -3 , and -10 dB attenuation (79%, 50%, 10% of the input power survives) at 59, 68, and 96 days^{-1} , respectively. Note that similar results are obtained if intraseasonal anomalies are estimated by high-pass filtering ($f_c = 90 \text{ days}^{-1}$) the original data with a Lanczos filter. The resulting intraseasonal variability is somewhat weaker though. On average over the central Peru region (86°W – 70°W ; 19°S – 10°S), the SST variability (RMS) for the anomalies calculated using the Lanczos filter with a cutoff frequency equals to $1/90 \text{ days}^{-1}$ are 6% weaker than the SST variability of the anomalies using the *Lin et al.*'s [2000] method.

3. SST-Wind Stress Modes Along the Coast

[16] Figure 1a shows the equatorward alongshore climatological wind stress amplitude along the Peruvian coast as derived from QuikSCAT satellite data. It exhibits two locations with a strong wind stress forcing favorable to upwelling that experiences maxima in Austral fall and winter: the Piura ($\sim 5^\circ\text{S}$) region and the central Peru region near Pisco ($\sim 15^\circ\text{S}$). These regions are also characterized by highly variable winds (Figure 1b). In particular, the Pisco region experiences wind bursts that share some characteristics with the so-called Coastal Jet off central Chile [Garreaud and Muñoz, 2005; K. Takahashi et al., in preparation, 2010].

[17] As a first step, the dominant patterns of covariability between wind stress and SST intraseasonal anomalies are estimated over the two regions that exhibit a peak in variability of the along shore winds. Two domains are outlined: the central Peru region (18.5°S – 10°S) near Pisco, considering a 5° width band along the coast, and the Piura region (8°S – 2°S ; 87°W – 79°W) in the northern Peru. The 5° width for the Pisco domain is chosen in order to reduce the influence of the offshore ocean variability in the south-

western quarter of the domain, not relevant for the study of coastal upwelling.

3.1. Pisco Region ($\sim 15^\circ\text{S}$)

[18] Figure 2 shows the results of the SVD between SST and wind stress over the Pisco region. A well defined dominant statistical mode of intraseasonal variability is evidenced: The mode captures 98% of the covariance (cf. Table 1). It consists in a near-coastal band of cool (warm) waters associated with equatorward (poleward) alongshore wind anomalies with a peak near $\sim 15^\circ\text{S}$. Whereas the first mode for SST accounts for 12% of the variance over the whole domain, its variance is confined in a narrow coastal fringe ($\sim 150 \text{ km}$ wide) and can peak locally as much as to 45%. For wind stress, the first mode accounts for a large amount of the explained variance (76%/78% for the zonal/meridional components) which traduces the larger spatial scale of the wind pattern and its connection with the subtropical pressure system variability at high frequency (see section 4.1). The maximum correlation (0.39) between the time series associated with the SVD modes for SST and wind stress peaks at a 0 day lag. The Figure 2c displays the global wavelet power spectrum [Torrence and Compo, 1998] of the SVD time series. A wide range of periods can be evidenced for both SST and wind stress ranging from 5 to 90 days. Two dominant period bands (we define the dominant period as that for which the power is 2 times larger than the confidence interval) can be evidenced for wind stress: (1) 10–25 days for which wind stress amplitude is comparable to that of SST (in adimensionalized unit) and (2) 35–60 days for which SST amplitude tend to be much larger than the wind stress amplitude (by an average factor of 10). The dominant period band for SST is 20–90 days with a peak at around 50 days. Noteworthy this spectral peak at ~ 50 days is present in both time series although most prominent in the SST time series. A similar 50 day peak

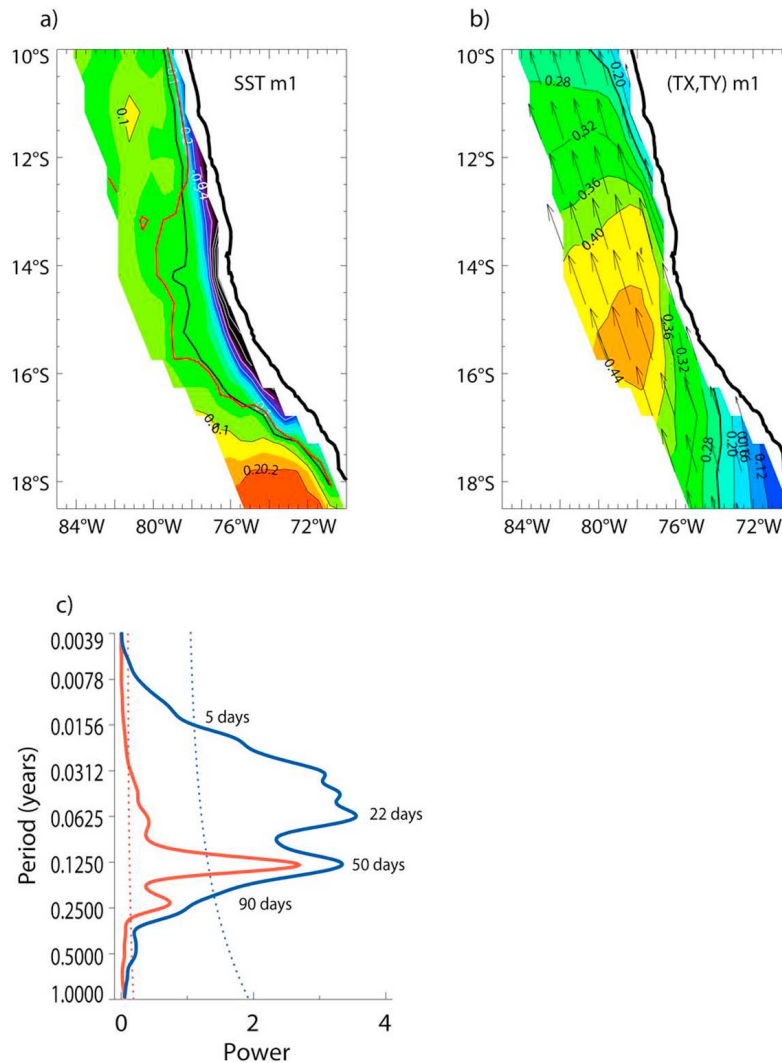


Figure 2. First mode of the SVD between wind stress and SST anomalies off central Peru: (a) SST and (b) wind stress amplitude/direction (color/arrows) spatial components. The black thick contour represents the zero contour for SST. The red contour corresponds to the zero contour for the results of the conditional SVD performed over the July–August–September season only. Contour is every 0.1 (0.04) unit for SST (wind stress). (c) The integrated wavelet spectrum of the associated time series for SST (red) and wind stress (blue) is presented. The power density of the SST time series was divided by 10 to fit the scale of wind stress. The dotted lines represent the 95% confidence interval estimated from a red noise (Markov).

has also been found off Chile, which has been attributed to the action of equatorial waves forced by intraseasonal wind variability [Hormazabal et al., 2001]. The spectrum also reveals a weaker peak at ~90 days for SST. The large magnitude of the ~50 day energy in the global wavelet spectrum indicates that coastal upwelling is significantly modulated

at this frequency. This peak also emerges clearly, above the 95% (90%) confidence level, from the density spectrum obtained from the Fourier transform of the autocorrelation function of the time series for SST (wind stress) (not shown). In section 4, we will investigate the large-scale (remote)

Table 1. Statistics Associated With the SVD Between SST Anomalies and Wind Stress Anomalies in the Pisco (15°S) and Piura (5°S) Regions

	Field	Explained Variance Mode 1	Covariance SVD Mode 1	Explained Variance Mode 2	Covariance SVD Mode 2
Pisco region	SST	12%	98%	7%	1%
	(tx, ty)	(78%, 76%)		(5%, 4%)	
Piura region	SST	13%	60%	14%	26%
	(tx, ty)	(16%, 42%)		(5%, 20%)	

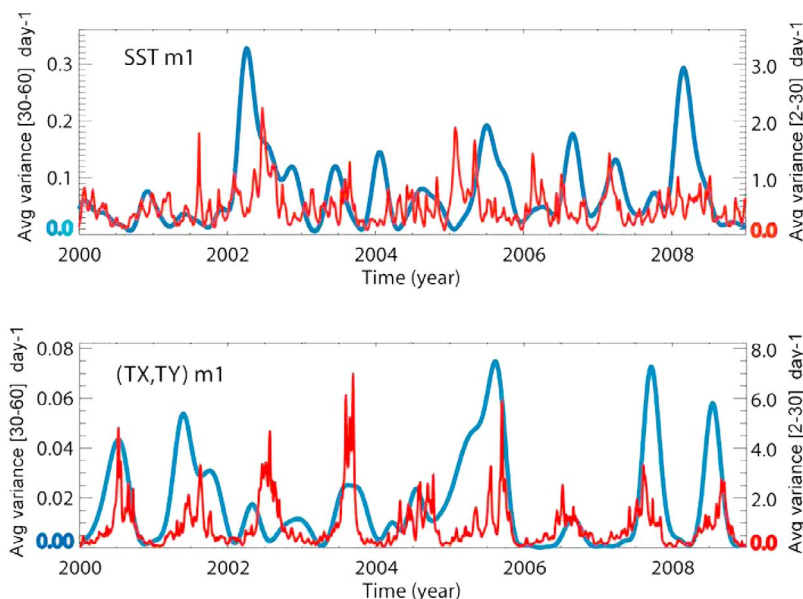


Figure 3. Scale-averaged wavelet power over the 2–30 day⁻¹ frequency band (red) and the 30–60 day⁻¹ frequency band (blue) of the time series associated with the dominant SVD mode for (top) SST and (bottom) wind stress.

forcing associated with the variability in these two frequency bands.

[19] Figure 3 shows the scale-averaged wavelet power time series for SST and wind stress over two period bands: 2–30 and 30–60 days. It confirms the two different regimes associated with these two timescales. First, note the marked seasonal cycle in the submonthly wind stress variability (Figure 3, bottom) with energy peaking in austral spring. This seasonal cycle is not as prominent in the SST submonthly variability. Still, the climatology of the 60 day running correlation between the SST and wind stress high-frequency time series ($f_c = 1/30 \text{ days}^{-1}$) peaks at 0.66 in August–September (cf. Figure 4, solid line) when high-frequency wind variability is maximum. This is consistent with SST anomalies induced by Ekman pumping associated with synoptic variability and stresses on the role of the August–September season for setting annual upwelling conditions. As a consistency check, the SVD between wind stress and SST anomalies was also carried out over the periods covering only the (July–August–September) JAS seasons. The patterns are similar to the ones presented in Figures 2a and 2b although with a larger amplitude for wind stress (not shown) and a further extension of the upwelling cell (front) in the Pisco region (see red contour in Figure 2a). Note also that the average squared coherence between wind stress and SST reach 0.51 in the 5–60 days⁻¹ frequency band over the whole period and 0.64 over the JAS seasons.

[20] For the 30–60 day period band, the scale-averaged power wavelet time series for SST and wind stress (Figure 3, blue lines) exhibit interannual fluctuations, with less clear phase relationship than for the 2–30 day period band. For instance, the year 2002 is characterized by large amplitude modulation in SST anomalies while wind stress amplitude is relatively weakly modulated. A reversal situation is found in 2005. The climatology of the 120 day running correlation for the low-pass filtered series ($f_c = 1/30 \text{ days}^{-1}$) is therefore low,

hardly significant except in Austral summer (cf. Figure 4, dotted line). This suggests that at these timescales, SST is not related in a straightforward manner to local wind stress. The results of a SVD performed on the SST and wind stress fields that have been previously low-pass filtered ($f_c = 1/30 \text{ days}^{-1}$) supports this interpretation. In particular, the obtained mode for SST does not exhibit a clear signature of coastal upwelling all along the coast of central Peru, whereas the wind stress pattern resembles the one of Figure 2b (not shown). Explained covariance is also low (11%).

[21] In the following we will refer to Central Peru Upwelling Index (CPUI) the time series of wind stress associated with the first SVD mode between wind stress and SST intraseasonal anomalies.

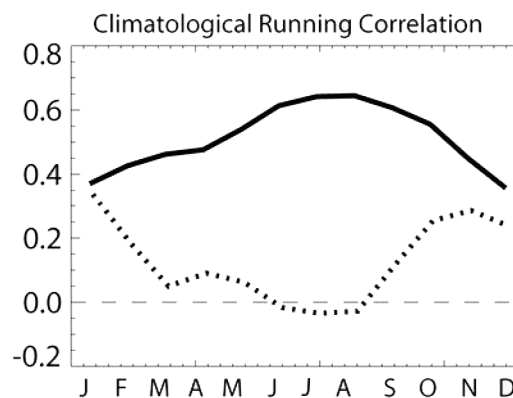


Figure 4. Climatology of the 60 day (120 day) running correlation between the SVD time series for SST and wind stress for two frequency bands. The solid (dotted) line is for the 1–30 day⁻¹ ([30, ∞] day⁻¹) frequency band. Correlation above 0.2 are significant at the level $\sigma = 95\%$.

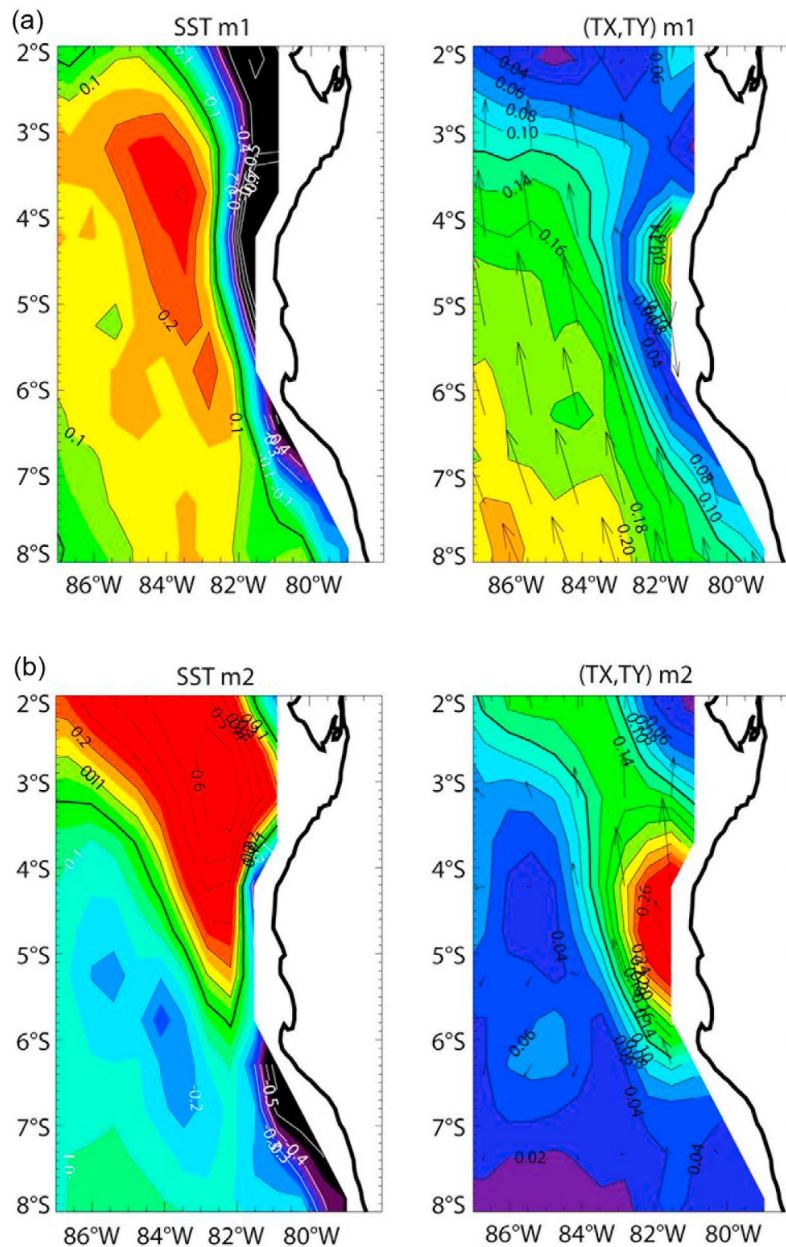


Figure 5. Spatial patterns of SST (left) and wind stress (right) for the (a) first and (b) second modes of the SVD between wind stress and SST intraseasonal anomalies off the Piura region. The contours for wind stress account for the amplitude and the arrows indicate the direction. The black thick contour represents the zero contour for SST. Contour is every 0.1 (0.02) unit for SST (wind stress).

3.2. Piura Region ($\sim 5^{\circ}\text{S}$)

[22] Similar analyses than above are performed for the northern Peru region near Piura which also exhibits significant intraseasonal variability in wind stress (Figure 1b). Figure 5 shows the results of the SVD between SST and wind stress anomalies. Conversely to the Pisco region, the intraseasonal variability consists in two dominant modes accounting for 60% and 26% of the covariance (cf. Table 1). The first mode shares some characteristics with the mode off the Pisco region (Figures 2a and 2b). For SST anomalies, a clear signature of coastal upwelling is evidenced with a zero contour following the 82°W meridian. Maximum

SST anomaly variability is found north of Piura. West of the 82°W meridian, during coastal upwelling events, a region of warm SST anomalies peaks at $(\sim 4^{\circ}\text{S}; 83^{\circ}\text{W})$. This warm anomaly pattern is not associated with positive Ekman pumping (not show), but rather likely correspond to the radiation of intraseasonal equatorial Rossby waves. This may explain why such warm anomalies does not extend as south as $\sim 7^{\circ}\text{S}$, which corresponds to the critical latitude of the 50 day equatorial Kelvin wave [Clarke and Shi, 1991] (see also section 4). As a consistency check of the trapping of the 50 day period, the spectrum of SST anomalies were estimated from 0 to 300 km off the Peruvian coasts and in

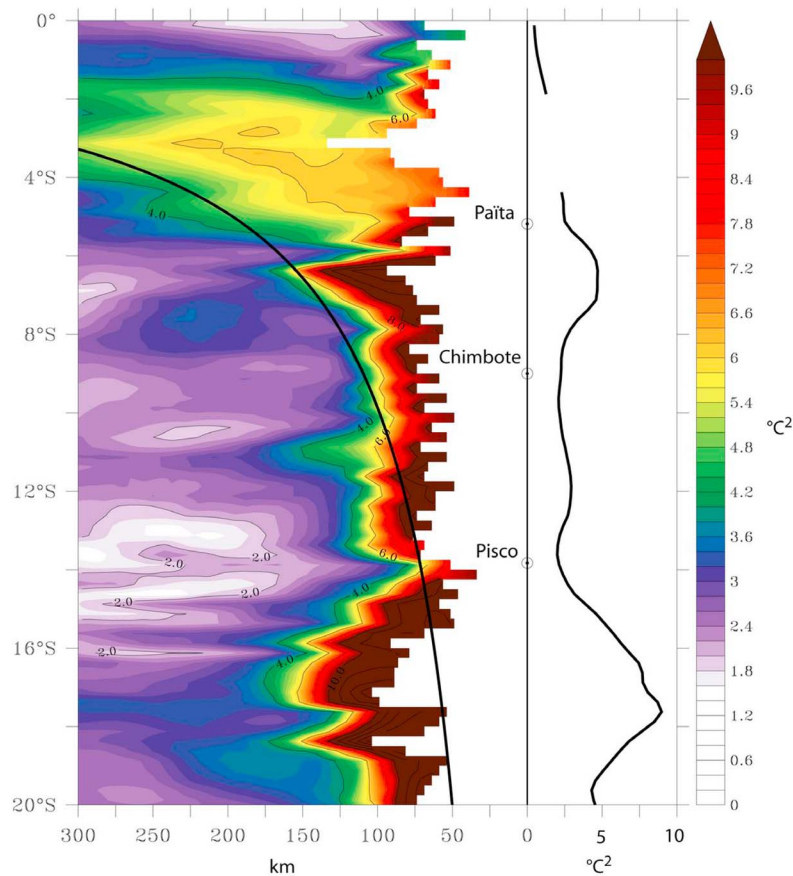


Figure 6. Energy peak at 50 days of the amplitude spectrum of SST anomalies ($^{\circ}\text{C}$) normal to the coast-line as a function of the distance to the coast (0–300 km) and the latitude (20°S – 0°N). Spectrum is estimated from the Fourier transform of the autocorrelation functions. The Rossby radius of deformation with $c = 2.5$ m/s is displayed by the black line on the left and indicates the characteristic cross-shore scale associated with the trapping of equatorial Kelvin wave. The average of energy at 50 days of the SST power spectrum ($^{\circ}\text{C}^2$) in the 100 km coastal fringe (smoothed using a 2° latitudinal running mean) is plotted on the right with a black line.

the direction normal to the coastline. The energy peak amplitude at ~ 50 days is presented in Figure 6. It clearly illustrates that the energy at the 50 day period tends to be confined near the coast from $\sim 7^{\circ}\text{S}$ consistently with the trapping of Kelvin waves south of the critical latitude. The characteristic cross-shore scale for the trapping of the equatorial Kelvin is indicated on Figure 6 as the distance from the coast given by the Rossby radius of deformation associated with the first baroclinic mode. Note that the Kelvin wave is trapped on the continental slope which may start as far as ~ 50 km from the coast (average value of the distance from the coast of the 200 m isobath between 8°S and 20°S) so that large energy can still be found as far as 150 km from the coast. Consistently with reduction of cross-shore scale of the trapped Kelvin wave as a function of latitude (decrease in the Rossby radius of deformation), there is an increase in energy at 50 days as a function of latitude (black line on the left-hand side of Figure 6).

[23] The second dominant SVD mode is distinct from the first one. Its pattern suggests that it accounts for the intraseasonal variability originating from the equatorial

region, with a tongue of warm (cold) waters penetrating southward as far as $\sim 7^{\circ}\text{S}$. South of this warm (cold) tongue, a cell of cold (warm) water is attached to the coast and shares similar characteristics than mode 1 in this region. The wind pattern associated to the warm tongue consists in a northward wind stress peak confined near the coast between 4°S and 5°S . The lag relationship between the associated time series for wind stress and SST indicates that SST anomalies precede wind stress anomalies (maximum correlation = 0.24 (0.39) at 1 day lag (for the SVD performed over the April–May–June (AMJ) seasons), and suggests that the winds respond to SST anomalies from equatorial origins consistently with the pattern of Figure 5b (right).

[24] The timescales of variability associated with the SVD modes for the Piura region are comparable for mode 1 and 2 (Figure 7), although the share of variance in the 1–30 day period band is larger for mode 1 than for mode 2, traducing a broader spectrum of variability in the high-frequency domain (i.e., $f > 1/30$ days $^{-1}$). Like for the Pisco region, a prominent energy peak at ~ 50 days is found for both fields and modes. Interestingly the 90 day peak is not present for

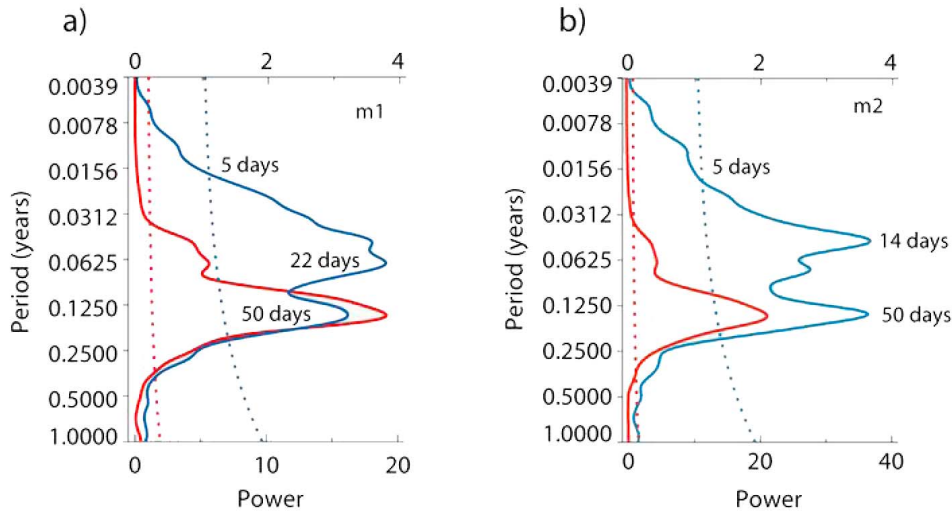


Figure 7. Global wavelet spectrum of the SST (red) and wind stress (blue) time series associated with the (a) first and (b) second SVD modes for the Piura region. The top (bottom) scale is for wind stress (SST). The dotted lines represent the 95% confidence interval estimated from a red noise (Markov).

the Piura region, suggesting that it results from equatorial wave forcing in the Piura region. Indeed, from linear theory, it is expected that the 90 day oscillation is trapped along the coast from its critical latitude estimated as $\sim 10^{\circ}\text{S}$ [Clarke and Shi, 1991] so that, north of 10°S , the 90 day variability radiates as Rossby waves which have zonal wavelength number too large to be grasp by the SVD over the domain considered here. On the other hand south of $\sim 10^{\circ}\text{S}$, the variability is trapped along the coast, which the SVD can capture.

[25] Like for the Piura region, the spectra of Figure 7 suggest two regimes, a first one associated with the high-frequency variability of wind stress, most prominent in mode 1 and a second one associated with the ~ 50 day period and its modulation, more relevant to mode 2. As an illustration of this later statement, the running correlation between the time series for SST and wind stress associated with modes 1 and 2 is presented in Figure 8 for periods shorter and higher than 30 days. Figure 8 indicates that the wind stress SST phase relationship for mode 1 is larger (smaller) for the frequencies smaller (larger) than $1/30 \text{ days}^{-1}$, whereas this is the opposite for mode 2. Note the peak of correlation in August–September for the submonthly frequencies of mode 1 ($c = 0.52$), likewise the one for the Piura region (Figure 4). For mode 2, maximum correlation for the signal associated with frequencies lower than $1/30 \text{ days}^{-1}$ is reached in November–December ($c = 0.50$) and the correlation values are low (hardly significant) all year around for the signal associated with the submonthly frequencies. Note that the peak of the correlation in austral summer for the “low”-frequency variability of mode 2 is consistent with the connexion of mode 2 with the MJO which peak activity season in the Southern Hemisphere is austral summer [Wheeler and Hendon, 2004]. This will be further discussed in section 4.2.

[26] As previously, we define the Northern Peru Upwelling Indices (NPUI) for the region of Piura as the time series of wind stress associated the first (NPUI1) and second (NPUI2)

SVD modes. Note that, by construction, NPUI1 and NPUI2 are independent (not correlated).

4. Link With Synoptic Variability

[27] Considering the characteristics of the spectrum of variability of the upwelling indices defined earlier, it is worth questioning to what extent the latter are associated with remote forcing. Whereas the 5–30 day range variability is likely to originate from extratropical storm activity, the 30–90 day range variability may have its source from tropical variability in the form of oceanic Kelvin waves and/or atmospheric disturbances like the MJO. In the following an attempt is made to quantify the relationship between these remote forcings and the upwelling indices as inferred from the above SVD analysis. The background hypothesis for interpreting the spectrum of the SVD results is that change in the rate of SST anomalies along the coast can be explained mostly by vertical advection. The latter can be induced rather through local Ekman pumping (i.e., $\frac{\partial T'}{\partial t} \approx -w'_{ek} \cdot \frac{\partial T}{\partial z}$ where w'_{ek} is the anomalous vertical velocity associated with Ekman

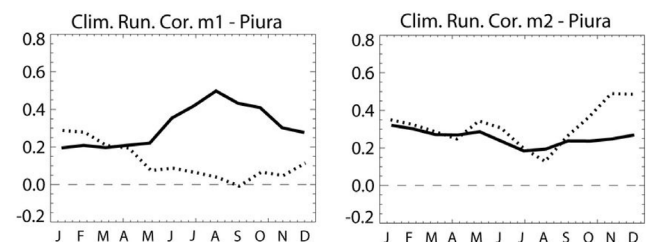


Figure 8. Climatology of the 60 day (120 day) running correlation between the SVD time series for SST and wind stress for modes (a) one and (b) two. The solid (dotted) line is for the 1–30 day ([30, ∞] day) period band. Correlation above 0.2 are significant at the level $\sigma = 95\%$.

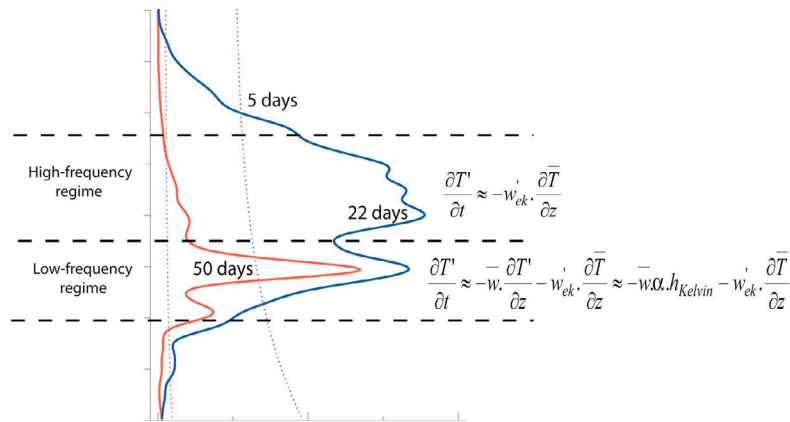


Figure 9. The two regimes of intraseasonal variability and the simplified equations for the interpretation of associated SST changes. The red and blue lines correspond to the global wavelet spectrum of Figure 2c. T' corresponds to the intraseasonal anomalies of SST, whereas \bar{T} stands for the monthly mean. Here w'_{ek} is the vertical velocity associated with Ekman pumping and \bar{w} is the mean upwelling rate. Anomalous vertical temperature ($\frac{\partial T'}{\partial z}$) can be related to thermocline depth anomalies (h_{Kelvin}) associated with the coastal-trapped Kelvin wave knowing the characteristics of the mean stratification along the coast that would allow deriving the coefficient α . It is then assumed that w'_{ek} is linked to some aspects of the large-scale atmospheric variability in the southeastern Pacific, whereas h_{Kelvin} is related to the equatorial Kelvin wave activity.

pumping, T' the anomalous SST and \bar{T} the mean SST) or through anomalous vertical temperature gradients associated with the crossing of coastal Kelvin wave (i.e., $\frac{\partial T'}{\partial t} \approx -\bar{w} \cdot \frac{\partial T'}{\partial z}$ where \bar{w} is the mean upwelling rate). According to the spectral analysis of the SVD modes, two main regimes can be identified: a high-frequency regime relevant for the direct impact of Ekman pumping, and a low-frequency regime which combines the effect of Ekman pumping and the displacement of the isotherms at the crossing of a coastal trapped Kelvin waves. The schematic of Figure 9 summarizes the background assumptions for interpreting the variability timescales of the SVD modes. Such assumptions will guide the analysis of the forcing mechanisms of the upwelling variability off Peru: Whereas the high-frequency regime is likely to be associated with the synoptic atmospheric variability (in particular the extratropical storm activity), the low-frequency regime may result from both the influence of equatorial intraseasonal Kelvin wave and MJO-modulated atmospheric disturbances. The following is devoted to the evaluation of these teleconnections.

4.1. Extratropical Storm Activity

[28] In order to illustrate the relationship between upwelling variability along the coast of Peru and the large-scale atmospheric variability, Figure 10 presents the map of the lagged linear regression coefficient of the SLP and near surface wind (U10m, V10m) anomalies with respect to the upwelling indices for Pisco (CPUI). The regression pattern features a positive SLP perturbation centered at (82°W; 30°S), which is located further to the west as in previous days, as indicated by the lag regressions patterns at 2, 4, and 6 days (SLP anomalies ahead CPUI). It indicates that the alongshore wind bursts off central Peru and associated upwelling are driven by the passage of an eastward moving migratory anticyclone, which results in an enhancement of the South Pacific anticyclone. Such pattern is similar to the

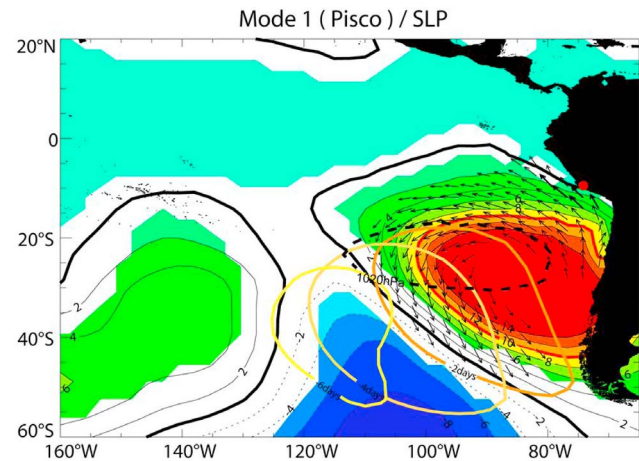


Figure 10. Map of the regression coefficients (r) of the SLP and (U10m, V10m) anomalies with respect to upwelling index in Pisco (CPUI). Here r is such that $SLP = p + r \cdot CPUI$, where p is a constant in time. The regression pattern therefore indicates the region where small changes in CPUI are associated with large changes in SLP, emphasizing the regions where the variability in SLP (surface circulation) is related (in the sense of the covariance) to the local winds in Pisco. The statistically significant regions (significant level >95%) are colored (see Appendix A for details). Units are hPa/CPUI unit for SLP and $ms^{-1}/CPUI$ unit for (U10m, V10m). The velocity field is only plotted for wind speed amplitude larger than 60% of the maximum amplitude. The contour 10 for SLP is in red. The equivalent contours for a lag regression at 2, 4, and 6 days (SLP ahead upwelling index) are in orange, beige, and yellow, respectively. The zero contour for SLP is a thick black line. The dashed thick black line indicates the mean position over the 2000–2008 period of the anticyclone and corresponds to the 1020 hPa isobath.

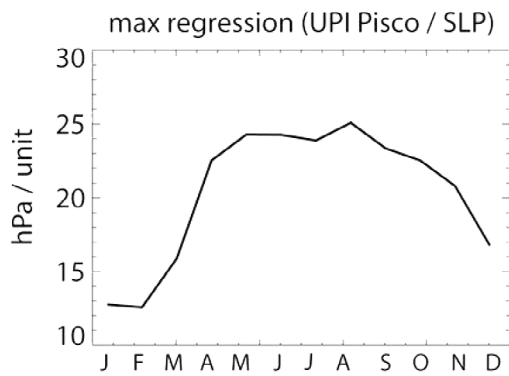


Figure 11. Maximum value over the region (120°W – 70°W ; 50°S – 10°N) of the regression between the upwelling index in Pisco (CPUI) and SLP as a function of calendar month. To calculate the regression value at a particular calendar month, a 3 month window centered on the 15th of the calendar month was selected for each year. The regression for each calendar month is thus performed over 24 months (8 years \times 3 months). Unit is hPa/CPUI unit.

one obtained for the upwelling index off central Chile [Renault *et al.*, 2009] although displaced $\sim 12^{\circ}$ to the north consistently with the difference in upwelling favorable season between the two regions (earlier in the year by 1–2 months for central Peru when the mean anticyclone is still close to its austral winter position). It was checked that such pattern is relevant for the 5–30 day period band by performing similar regression analysis for the high-passed filtered signal (not shown). For the 30–60 day period band, the regression pattern is somewhat similar although with a much weaker amplitude traducing a different forcing mechanism of the upwelling variability in this period band (see section 4.2). As an attempt to identify the favorable season for the connection between the South Pacific anticyclone high-frequency variability and CPUI, the lagged regression analysis was performed for each calendar month. A 3 month window centered on the calendar month was selected for each individual years leading to bins of 24 months for calculating the regression coefficients. The pattern for each calendar month is similar to the one of Figure 10 except that the magnitude of the regression varies from month to month, reflecting changes in the “strength” of the relationship between local wind/SST anomalies and synoptic variability. It exhibits a strong seasonal cycle as illustrated in Figure 11 with the maximum regression value at lag 0 in the region (50°S – 10°S ; 120°W – 80°W). It indicates that favorable season for such teleconnection extends from April to October, which corresponds to the seasonal equatorward migration of the anticyclone.

[29] Similar pattern is obtained for the upwelling index at Piura corresponding to the SVD mode 1 confirming the in-phase relationship between the upwelling at Pisco and Piura (not shown). The regression pattern for the upwelling index at Piura corresponding to the SVD mode 2 (Figures 5a, bottom and 5b, bottom) is also associated with migratory depressions associated with upwelling favorable condition along the coast, also with weaker values of regression coefficients.

4.2. MJO-Type Variability

[30] Even though the MJO is most evident in the global tropics, it is also connected to substantial variations of mid- and high-latitude atmospheric circulation [Vecchi and Bond, 2004]. There is considerable evidence that deep tropical atmospheric convection impacts atmospheric flow in the extratropics. Whereas much attention has been paid to the connexion between intraseasonal variability of the tropics with the midlatitudes of the Northern Hemisphere, little has been documented for the midlatitudes of the Southern Hemisphere, in particular in the eastern South Pacific where the low SST does not allow for deep convection. The mechanisms of transmission of the MJO signals to the mean circulation in the off-equatorial region remain actually unclear and controversial. Meridional propagation of the MJO appears to be the primary mechanism by which the MJO impacts the Indian [Yasunari, 1981; Krishnamurti and Subrahmanyam, 1982] and Australian [Matthews *et al.*, 1996] summer monsoons. The impact over regions west of the source regions of the MJO can take place through a number of processes (see the introduction of Berbery and Nogues-Paegle [1993]). The difficulty to identify a clear mechanism lies in part to the fact that the MJO is not strictly periodic but has a preferred timescale of about 30–60 days and its associated teleconnexion pattern has a significant seasonal dependence [Hendon *et al.*, 2007]. Thus no significant correlation could be found between several modes of the intraseasonal variability in the tropics (e.g., 16–18 and 21–28 day band) and the Southern Hemisphere extratropics [Ghil and Mo, 1991]. On the other hand, significant correlations between tropics and extratropics have been found in the 30–70 day band during winter but not summer [Knutson and Weickmann, 1987].

[31] Here, we investigate to which extend the variability in the 30–90 day period band of the upwelling indices at Pisco and Piura can be related to the large-scale atmospheric circulation, considering that their spectrum exhibit a prominent period peak around 50 days (Figures 2c and 7). Whereas such variability can originate from a direct tropical atmospheric connexion from the western equatorial Pacific (where MJO is the most active) to the eastern tropical Pacific, our results support the hypothesis that MJO-type variability rather impacts the midlatitudes pressure system in the central Pacific, which in turn, through the modulation of westward propagating extratropical disturbances, influences the southeastern Pacific anticyclone. As a consistency check of this later statement, the Figure 12 shows the spectrum of the time series associated with the EOF of along shore wind stress anomalies off Pisco and of the total SLP over the region encompassing the seasonal variability of the South Pacific High (40°S – 15°S ; 120°W – 80°W). Anomalies are here relative to the mean seasonal cycle for wind stress. Both spectra exhibit a clear peak in the 40–60 day period range indicating that energetic upwelling variability at 50 days may also originates from local atmospheric forcing.

[32] In order to quantify the relationship between large-scale atmospheric variability and the upwelling variability in Pisco, Figure 13 presents the regression map between CPUI and SLP (U10m, V10m) anomalies as a function of the calendar month in order to grasp the seasonal dependence between CPUI and MJO. Maximum regression in the sur-

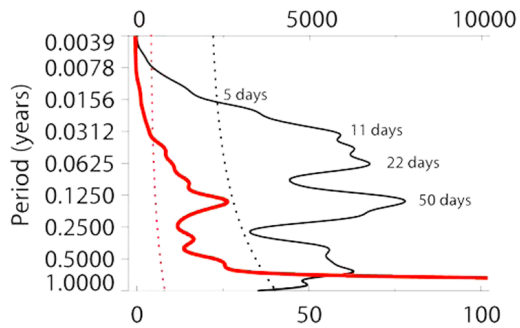


Figure 12. Global wavelet spectrum of the time series associated with the first EOF of the zonal and meridional wind stress anomalies off the coast in central Peru (same domain than the one of Figure 2b, black line) and of the total SLP over the region (40°S – 15°S ; 120°W – 80°W , red line). The anomalies for wind stress are relative to the mean seasonal cycle. The dotted lines represent the 95% confidence interval estimated from a red noise (Markov). The top scale is for SLP and the bottom scale is for the zonal and meridional wind stress. Unit is adimensionalized. The EOF accounts for 89% and 72% of the explained variance for wind stress anomalies and SLP, respectively.

roundings of the southeastern Pacific anticyclone is found for the months of March, April, and May which corresponds to the season of maximum MJO activity in the Southern Hemisphere delayed by ~ 2 months [Wheeler and Hendon, 2004]. It suggests a possible connection between MJO-type variability and the southeastern Pacific anticyclone and that the later can influence the upwelling variability off Peru. It is beyond the scope of the present paper to investigate the mechanisms of teleconnection between MJO and extratropical variability. It is, however, interesting to note here that the reason why the 50 day period emerges that clearly from the SVD analysis (Figures 2 and 7) may actually results from a dual remote forcings: (1) from the midlatitudes through the southeastern Pacific anticyclone fluctuations and (2) from the equator in the forms of oceanic equatorial intraseasonal Kelvin waves.

4.3. Equatorial Wave Forcing

[33] The spectrum of the equatorial Kelvin wave in the Pacific exhibits a wide range of frequencies in the intraseasonal band [cf. Dewitte *et al.*, 2008]. Whereas the 50–70 and the 100–120 day period band are the ones that have the largest amplitude, the higher-frequency band (although less energetic) are also of interest in this study because it is trapped from 5°S and as so, show up in the SVD results. Note that for lower frequency, part of the energy has to radiate as Rossby wave that have large zonal wavelength so that associated coastal variability have a basin-scale pattern and cannot reflect the coastal upwelling. The intraseasonal equatorial

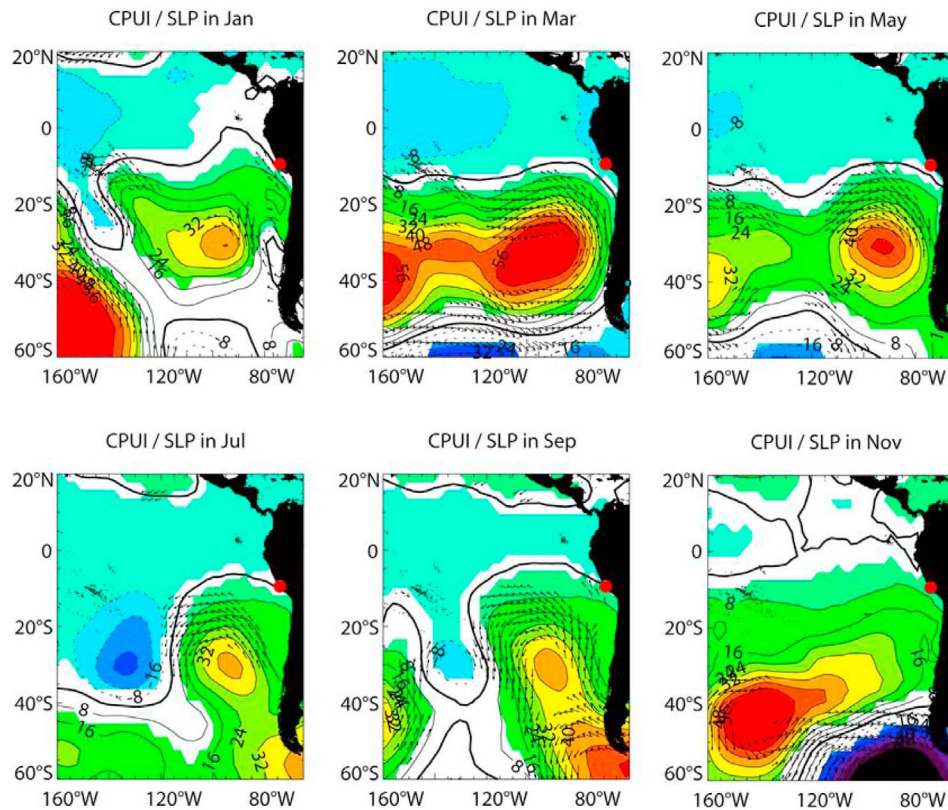


Figure 13. Same as Figure 10 but for the low-pass filtered SVD time series and as a function of calendar month. A 3 month window centered on the 15th of the calendar month was selected for each year so that regression for each calendar month is performed over 24 months.

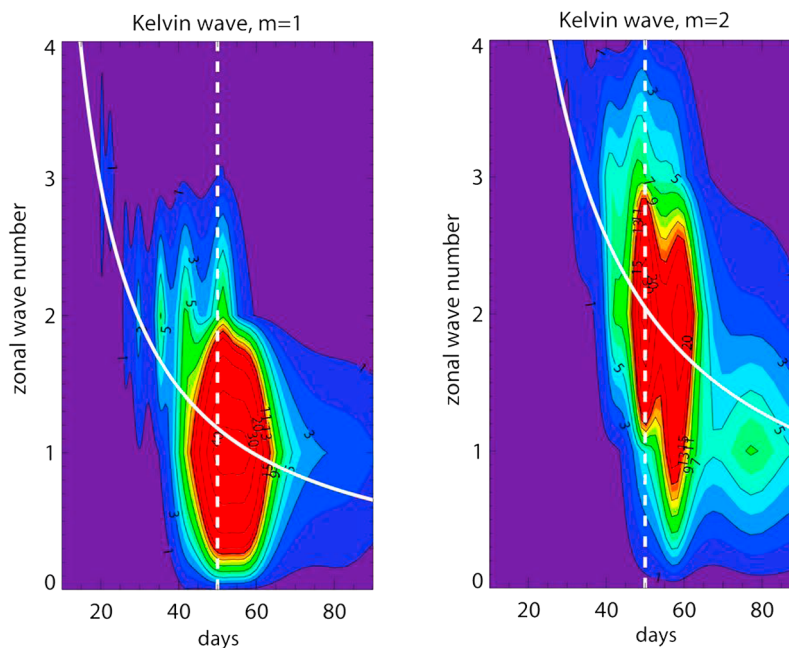


Figure 14. The space-time power spectral density of the intraseasonal Kelvin (at the equator) wave for the (left) first and (right) second baroclinic modes. Theoretical dispersion curves for Kelvin waves using the zonally averaged phase velocity over the equatorial Pacific as derived from the vertical mode decomposition of the mean stratification are plotted by a thick white line. Units are cm^4 for mode 1 and 0.2 cm^4 for mode 2. The dashed white vertical line indicates the 50 day period.

Kelvin wave is forced to a large extent by the MJO and/or atmospheric convective Kelvin waves [Roundy and Kiladis, 2006] and projects preferentially on the first two baroclinic modes [Dewitte et al., 2008].

[34] A bivariate space-time spectral analysis [Hayashi, 1982] is performed on the first two baroclinic modes of the equatorial Kelvin wave as derived from the Mercator simulation. The Figure 14 presents the resulting spectrum in the zonal wavelength and period space. It indicates that in the frequency band of interest, the zonal wave number 2 (1) is favored especially for baroclinic mode 2 (1). Not surprisingly the first two modes exhibit a peak energy at ~ 50 days indicating that they are largely forced by the MJO [Roundy and Kiladis, 2006]. Note the well defined energy maximum of the second baroclinic mode Kelvin wave. The Kelvin wave amplitude at 85°W of the first two modes is first compared to the MJO index (Figure 15a) using a lagged correlation analysis, which provides an estimate of the time for the waves to travel across the Pacific. The Figure 15a indicates that it takes ~ 55 and ~ 90 days for the first and second baroclinic modes Kelvin wave, respectively, to travel from $\sim 145^\circ\text{E}$ (source of the MJO forcing) to 85°W . This is consistent with the free propagation of Kelvin wave with averaged phase speed typical of the central equatorial Pacific ($c_1 \sim 2.8 \text{ ms}^{-1}$ and $c_2 \sim 1.7 \text{ ms}^{-1}$). Because of the difference in phase speed of the baroclinic modes, the impact of the Kelvin wave on the upwelling variability is not straightforward. The modes can also undergoes change in amplitude and propagating characteristics as they propagates from west to east because of the zonal change in stratification associated with the sloping equatorial thermocline [Busalacchi and Cane, 1988; Dewitte et al., 1999]. In order to assess the relationship

between MJO (Kelvin wave forcing in the western equatorial Pacific) and the upwelling variability off the coast of Peru, the lag correlation between the MJO index and the upwelling indices as defined in section 3 is estimated (Figure 15b). It indicates that only NPUI2 relates clearly to the MJO with a maximum correlation ($c = 0.50$) encountered at lag 95 days, which indicates a privileged role of the second baroclinic Kelvin wave (a 5 day delay is assumed for the wave to reach 5°S from 145°E along the equator and then along the coast). The relatively low correlation between the MJO index and the other upwelling indices (NPUI1 and PCUI) suggests that the baroclinic modes can interfere destructively on the upwelling variability. As a complementary test, the regression between the Kelvin wave and the upwelling indices is estimated as a function of longitude (Figures 15c–15e). This highlights the eastward propagation of the Kelvin waves and its relationship at the eastern boundary with the upwelling variability. The sinusoidal shape of the regression curves accounts for the eastward propagation of the Kelvin wave. It is clear for all indices for the first baroclinic mode. For the second baroclinic mode, it is well defined in the eastern part of the equatorial Pacific because the second baroclinic mode experiences an increase in amplitude in the eastern Pacific due to the shallower thermocline there [Dewitte et al., 1999, 2008]. Figures 15c–15e also provide the phase relationship at the eastern boundary between the Kelvin wave and the upwelling indices. It indicates that, except for NPUI2, the first and second baroclinic mode Kelvin waves have an opposite impact on the upwelling indices. For NPUI2, the regression value is relatively large (positive) for mode 2 and almost zero for mode 1. This suggests that NPUI2 is related to the second baroclinic mode Kelvin wave (correlation value between

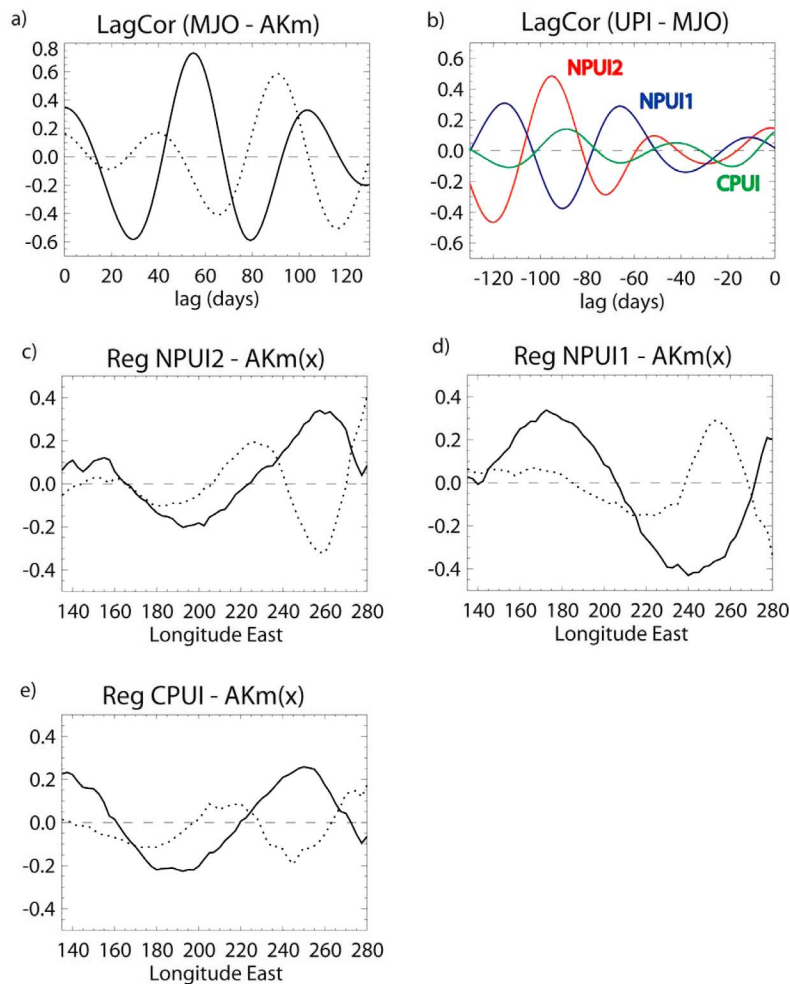


Figure 15. Lagged correlation (a) between the MJO index and the equatorial oceanic Kelvin wave amplitude at 85°W (baroclinic mode 1 (solid) and baroclinic mode 2 (dotted)) and (b) between the MJO index and the upwelling indices (SST mode 2 at Piura (red), SST mode 1 in Piura (blue), and SST mode 1 in Pisco (green)). (c–e) Regression value between the upwelling indices and the equatorial Kelvin wave along the equator. Units are in cm per unit of the upwelling index.

NUPI2 and the second baroclinic mode Kelvin wave at 80°W reaches 0.42), whereas NUPI1 and CPUI are only modulated at different time by the first and second baroclinic mode Kelvin waves.

5. Discussion and Conclusions

[35] The alongshore wind stress and SST intraseasonal variability was documented based on a long-term record of high-resolution satellite data. Regions of significant intraseasonal variability are found: one off Piura ($\sim 5^{\circ}\text{S}$) in the northern Peru and the other one off central Peru in the Pisco ($\sim 15^{\circ}\text{S}$) region. The latter has the most pronounced variability with a seasonal cycle mimicking the alongshore winds seasonal cycle (namely stronger/weaker in austral winter/summer). Variability timescales range from 2 to 90 days with two main distinct period bands, namely, 10–25 and 35–60 days. A covariance analysis (SVD) reveals that a significant variance of the SST anomalies along the coast is associated with the direct forcing by the wind stress. In the Pisco region, the dominant mode (98% of the covariance) of

SST anomalies consists in an elongated band of cooler/warmer waters that extends offshore more near Pisco than south and north of it. In the Piura region, two dominant modes emerge: the first one associated with upwelling variability forced by the alongshore winds and the second one associated with the incursion of warm equatorial waters into the coastal system. The second mode in Piura is associated with intraseasonal oceanic Kelvin waves and to the radiation of the reflected Rossby wave north of the critical latitude. The covariance analysis reveals that the wind stress pattern of this mode is characteristic of the direct response of the low-level circulation (*Lindzen and Nigam's* [1987] model type) to local SST anomalies.

[36] The covariance analysis also reveals a well defined energy peak around the 50 day period. This peak cannot be accounted for just Ekman dynamics. It is not an artifact of filtering since it is also prominent in the “raw” (unfiltered) data. It is shown that it is associated with the intraseasonal Kelvin wave of the first and second baroclinic modes. Because the variability of the SLP system in the midlatitudes also exhibits a peak variability at 50 days (Figure 12),

there is the possibility of a destructive/constructive interaction of coastal SST anomalies induced by the oceanic Kelvin wave and by the modulation of the SLP system in the mid-latitudes in the 30–60 day period band. Whether the latter variability results from tropical–extratropical teleconnections involving the MJO or is part of the extratropical internal variability will need further investigation. The investigation of the mechanisms of connexion between the MJO and the regional circulation off Peru is beyond the scope of this paper. At this stage, in the light of our analysis, it is interesting to note that such mechanism may involve the extratropical response to MJO forcing of the anomalous circulation in the form of subtropical Rossby wave propagation, consistently with former studies [Matthews *et al.*, 1996]. Considering the current lack of knowledge of the actual mechanisms connecting tropical variability (MJO type) and the mean circulation in the extratropical latitudes of the Southern Hemisphere [Berbery and Nogues-Paegle, 1993], our results call for research efforts in that direction.

[37] At lower periods (10–25 days), the upwelling variability exhibits a clear relationship with the large-scale atmospheric variability with a marked seasonal cycle (stronger in Austral winter). In particular, the alongshore wind bursts off central Peru and associated upwelling are related to the SEP anticyclone moving toward the Peru coasts from the central Pacific. Such connection may result from the weakening of South Pacific High due to the equatorward shift of the midlatitude depressions and their penetration in the system of high pressure. These depressions apparently divide the South Pacific anticyclone in two parts with the eastern part moving toward Peru. Such mechanism needs to be investigated.

[38] Overall our results illustrate the potential of satellite data for investigating upwelling variability off the coast in regions of the world where the scarcity and quality of the available in situ data remains a limitation. Those results are also aimed to serve as a benchmark for the validations of high-resolution regional models, despite the relatively low resolution of the data used in this study. As higher resolution data sets will become available in the future (GHRSSST, ASCAT, 12.5 km reprocessed QuikSCAT winds), similar analyses could be performed in order to document the intraseasonal upwelling variability in the nearshore domain (beyond the QuikSCAT blind zone). This may certainly lead to improve our knowledge of the dynamics of this region because alongshore winds can experience drastic change near the coast (cf. Capet *et al.* [2004] for the California system). Higher-resolution wind data will be also useful for high-resolution modeling of eastern boundary current systems.

Appendix A: Confidence Level for Regression

[39] A “Student’s *t*” test is used [Spiegel, 1990] to compute the confidence level for the regression. As a first step, the standard error of the slope (SE) is calculated as follows:

$$SE = \sqrt{\frac{\sum (y_i - \hat{y}_i)^2 / n - 2}{\sum (x_i - \bar{x})^2}}$$

where y_i is the value of the dependent variable for the observation i , \hat{y}_i is the corresponding estimated value of the dependent variable for the observation i , x_i is the observed value of the independent variable for the observation i , \bar{x} is the mean of the independent variable, and n is the number of observations.

The statistic $t = b/SE$ (where b is the slope) is assumed to have student’s distribution with degree of freedom df taken as $n - 2$.

[40] **Acknowledgments.** Gilles Garric (Mercator) is acknowledged for providing the Mercator outputs for deriving the contribution of the equatorial Kelvin waves. Yamina Silva (IGP) is thanked for her support at the early stage of this study. Jorge Vasquez (JPL) is also thanked for fruitful discussions. The authors are grateful to Dimitri Gutierrez (codirector of the LMI DISCOH) for his support during the course of this study. The three anonymous reviewers are thanked for their constructive comments and suggestions that helped to improve the manuscript.

References

- Bakun, A. (1990), Global climate change and intensification of coastal upwelling, *Science*, *247*, 198–201, doi:10.1126/science.247.4939.198.
- Bakun, A., and S. J. Weeks (2008), The marine ecosystem off Peru: What are the secrets of its fishery productivity and what might its future hold?, *Prog. Oceanogr.*, *79*, 290–299, doi:10.1016/j.pocean.2008.10.027.
- Berbery, E. H., and J. Nogues-Paegle (1993), Intraseasonal interactions between the tropics and extratropics in the Southern Hemisphere, *J. Atmos. Sci.*, *50*, 1950–1965, doi:10.1175/1520-0469(1993)050<1950:IIBTTA>2.0.CO;2.
- Bograd, S. J., I. Schroeder, N. Sarkar, X. Qiu, W. J. Sydeman, and F. B. Schwing (2009), Phenology of coastal upwelling in the California Current, *Geophys. Res. Lett.*, *36*, L01602, doi:10.1029/2008GL035933.
- Bretherton, C. S., C. Smith, and J. M. Wallace (1992), An intercomparison of methods for finding coupled patterns in climate data, *J. Clim.*, *5*, 541–560, doi:10.1175/1520-0442(1992)005<0541:AIOMFF>2.0.CO;2.
- Brink, K. H., J. S. Allen, and R. L. Smith (1978), A study of low-frequency fluctuations near the Peru coast, *J. Phys. Oceanogr.*, *8*, 1025–1041, doi:10.1175/1520-0485(1978)008<1025:ASOLFF>2.0.CO;2.
- Busalacchi, A. J., and M. A. Cane (1988), The effect of varying stratification on low-frequency equatorial motions, *J. Phys. Oceanogr.*, *18*, 801–812, doi:10.1175/1520-0485(1988)018<0801:TEOVSO>2.0.CO;2.
- Capet, X., P. Marchesiello, and J. McWilliams (2004), Upwelling response to coastal wind profiles, *Geophys. Res. Lett.*, *31*, L13311, doi:10.1029/2004GL020123.
- Carr, M.-E. (2001), Estimation of potential productivity in eastern boundary currents using remote sensing, *Deep Sea Res. Part II*, *49*, 59–80, doi:10.1016/S0967-0645(01)00094-7.
- Carton, J. A., and B. S. Giese (2008), A reanalysis of ocean climate using Simple Ocean Data Assimilation (SODA), *Mon. Weather Rev.*, *136*, 2999–3017, doi:10.1175/2007MWR1978.1.
- Centre ERS d’Archivage et de Traitement (2002), QuikSCAT scatterometer mean wind field products user manual, *Rep. C2-MUT-W-04-IF*, Brest, France. [Available at ftp://ftp.ifremer.fr/ifremer/cersat/documentation/gridded/mwv-quikscat/mwv_vol2.pdf.]
- Chelton, D. B., S. K. Esbensen, M. G. Schlax, N. Thum, M. H. Freilich, F. J. Wentz, C. L. Gentemann, M. J. McPhaden, and P. S. Schopf (2001), Observations of coupling between surface wind stress and sea surface temperature in the eastern tropical Pacific, *J. Clim.*, *14*, 1479–1498, doi:10.1175/1520-0442(2001)014<1479:OOCBSW>2.0.CO;2.
- Clarke, A. J., and C. Shi (1991), Critical frequencies at ocean boundaries, *J. Geophys. Res.*, *96*, 10,731–10,738, doi:10.1029/91JC00933.
- Colas, F., X. Capet, J. C. McWilliams, and A. Shchepetkin (2008), 1997–98 El Niño off Peru: A numerical study, *Prog. Oceanogr.*, *79*, 138–155, doi:10.1016/j.pocean.2008.10.015.
- Cornejo-Rodríguez, M. P., and D. B. Enfield (1987), Propagation and forcing of high-frequency sea level variability along the west coast of South America, *J. Geophys. Res.*, *92*, 14,323–14,334, doi:10.1029/JC092iC13p14323.
- Croquette, M., G. Eldin, C. Grados, and M. Tamayo (2007), On differences in satellite wind products and their effects in estimating coastal upwelling processes in the south-east Pacific, *Geophys. Res. Lett.*, *34*, L11608, doi:10.1029/2006GL027538.
- Dewitte, B., G. Reverdin, and C. Maes (1999), Vertical structure of an OGCM simulation of the equatorial Pacific Ocean in 1985–1994, *J. Phys. Oceanogr.*, *29*, 1542–1570, doi:10.1175/1520-0485(1999)029<1542:VSOAOS>2.0.CO;2.
- Dewitte, B., S. Illig, L. Parent, Y. duPenhoat, L. Gourdeau, and J. Verron (2003), Tropical Pacific baroclinic mode contribution and associated long waves for the 1994–1999 period from an assimilation experiment with altimetric data, *J. Geophys. Res.*, *108*(C4), 3121, doi:10.1029/2002JC001362.
- Dewitte, B., M. Ramos, O. Pizarro and G. Garric (2007), Connexion between the equatorial Kelvin wave and the extra-tropical Rossby wave in the south eastern Pacific in the Mercator Ocean POG05B simulation: A case study for the 1997/98 El Niño, *Mercator Ocean Q. Newsl.*, *26*, 34–44.
- Dewitte, B., S. Purca, S. Illig, L. Renault, and B. Giese (2008), Low frequency modulation of the intraseasonal equatorial Kelvin wave activity in the

- Pacific Ocean from SODA: 1958–2001, *J. Clim.*, *21*, 6060–6069, doi:10.1175/2008JCLI2277.1.
- Ekman, V. W. (1905), On the influence of the Earth's rotation on ocean currents, *Ark. Mat. Astron. Fys.*, *11*(2), 1–52.
- Enfield, D. B. (1981), Annual and no seasonal variability of monthly low level wind fields over the southeastern tropical Pacific, *Mon. Weather Rev.*, *109*, 2177–2190, doi:10.1175/1520-0493(1981)109<2177:AANVOM>2.0.CO;2.
- Enfield, D. B., M. P. Cornejo-Rodríguez, R. L. Smith, and P. A. Newberger (1987), The equatorial source of propagating variability along the Peru coast during the 1982–1983 El Niño, *J. Geophys. Res.*, *92*, 14,335–14,346, doi:10.1029/JC092iC13p14335.
- Fox-Kemper, B., and R. Ferrari (2008), Parameterization of mixed layer eddies. Part II: Prognosis and impact, *J. Phys. Oceanogr.*, *38*, 1166–1179, doi:10.1175/2007JPO3788.1.
- Fox-Kemper, B., R. Ferrari, and R. W. Hallberg (2008), Parameterization of mixed layer eddies. Part I: Theory and diagnosis, *J. Phys. Oceanogr.*, *38*, 1145–1165, doi:10.1175/2007JPO3792.1.
- Garreaud, R., and R. Muñoz (2005), The low-level jet off the subtropical west coast of South America: Structure and variability, *Mon. Weather Rev.*, *133*, 2246–2261, doi:10.1175/MWR2972.1.
- Garric, G., R. Bourdalle-Badie, O. Le Galloudec, C. Bricaud, C. Derval, E. Durand, and Y. Drillet (2008), Description of the interannual experiment ORCA025–T09, 1998–2006, *Mercator Ocean Rep.* 235, Groupe d'Intérêt Public Mercator Ocean, Ramonville St Agne, France.
- Gentemann, C. L., C. J. Donlon, A. Stuart-Menteth, and F. J. Wentz (2003), Diurnal signals in satellite sea surface temperature measurements, *Geophys. Res. Lett.*, *30*(3), 1140, doi:10.1029/2002GL016291.
- Ghil, M., and K. Mo (1991), Intraseasonal oscillations in the global atmosphere. Part II: Southern Hemisphere, *J. Atmos. Sci.*, *48*, 780–790, doi:10.1175/1520-0469(1991)048<0780:IOITGA>2.0.CO;2.
- Gushchina, D. Y., B. Dewitte, and S. A. Korkmazova (2010), Intraseasonal variability in an intermediate complexity atmospheric model, *Russ. Meteorol. Hydrol.*, *35*(4), 237–252, doi:10.3103/S1068373910040011.
- Gutiérrez, D., E. Enriquez, S. Purca, L. Quipuzcoa, R. Marquina, G. Flores, and M. Graco (2008), Oxygenation episodes on the continental shelf of central Peru: Remote forcing and benthic ecosystem response, *Prog. Oceanogr.*, *79*, 177–189, doi:10.1016/j.pcean.2008.10.025.
- Halpern, D. (2002), Offshore Ekman transport and Ekman pumping off Peru during the 1997–1998 El Niño, *Geophys. Res. Lett.*, *29*(5), 1075, doi:10.1029/2001GL014097.
- Hayashi, Y. (1982), Space-time spectral analysis and its applications to atmospheric waves, *J. Meteorol. Soc. Jpn.*, *60*, 156–171.
- Hendon, H. H., B. Liebmann, and J. D. Glick (1999), Interannual variability of the Madden–Julian Oscillation during austral summer, *J. Clim.*, *12*, 2538–2550, doi:10.1175/1520-0442(1999)012<2538:IVOTMJ>2.0.CO;2.
- Hendon, H. H., M. C. Wheeler, and C. Zhang (2007), Seasonal dependence of the MJO–ENSO relationship, *J. Clim.*, *20*, 531–543, doi:10.1175/JCLI4003.1.
- Hormazábal, S., G. Shaffer, J. Letelier, and O. Ulloa (2001), Local and remote forcing of sea surface temperature in the coastal upwelling system off Chile, *J. Geophys. Res.*, *106*, 16,657–16,671, doi:10.1029/2001JC900008.
- Illig, S., B. Dewitte, C. Périgaud, and C. Derval (2007), Equatorial wave intra-seasonal variability in the Indian and Pacific oceans in the Mercator Ocean POG05B simulation, *Mercator Ocean Q. Newsl.*, *26*, 45–56.
- Kalnay, E., et al. (1996), The NCEP/NCAR 40-year reanalysis project, *Bull. Am. Meteorol. Soc.*, *77*, 437–471, doi:10.1175/1520-0477(1996)077<0437:TNYRP>2.0.CO;2.
- Kessler, W. S., and R. Kleeman (2000), Rectification of the Madden–Julian Oscillation into the ENSO cycle, *J. Clim.*, *13*, 3560–3575, doi:10.1175/1520-0442(2000)013<3560:ROTMJO>2.0.CO;2.
- Knutson, T. R., and K. M. Weickmann (1987), 30–60 days atmospheric oscillations: Composite life cycle of convection and circulation anomalies, *Mon. Weather Rev.*, *115*, 1407–1436, doi:10.1175/1520-0493(1987)115<1407:DAOCLC>2.0.CO;2.
- Krishnamurti, T. N., and D. Subrahmanyam (1982), The 30–50 day mode at 850 mb during MONEX, *J. Atmos. Sci.*, *39*, 2088–2095, doi:10.1175/1520-0469(1982)039<2088:TDMAMD>2.0.CO;2.
- Lin, J.-L., et al. (2006), Tropical intraseasonal variability in 14 IPCC AR4 climate models: Part I: Convective signals, *J. Clim.*, *19*, 2665–2690, doi:10.1175/JCLI3735.1.
- Lin, J. W.-B., J. D. Neelin, and N. Zeng (2000), Maintenance of tropical intraseasonal variability: Impact of evaporation–wind feedback and mid-latitude storms, *J. Atmos. Sci.*, *57*, 2793–2823, doi:10.1175/1520-0469(2000)057<2793:MOTIV1>2.0.CO;2.
- Lindzen, R. S., and S. Nigam (1987), On the role of sea surface temperature gradients in forcing low-level winds and convergence in the tropics, *J. Atmos. Sci.*, *44*, 2418–2436, doi:10.1175/1520-0469(1987)044<2418:OTROSS>2.0.CO;2.
- Madden, R. A., and P. R. Julian (1994), Observations of the 40–50-day tropical oscillation—A review, *Mon. Weather Rev.*, *122*, 814–837, doi:10.1175/1520-0493(1994)122<0814:OOTDTO>2.0.CO;2.
- Madec, G., P. Delecluse, M. Imbard, and C. Levy (1998), OPA 8.1 tracer model reference manual, report, 91 pp., Inst. Pierre Simon Laplace, Paris.
- Matthews, A. J., B. J. Hoskins, J. M. Slingo, and M. Blackburn (1996), Development of convection along the SPCZ within a Madden–Julian Oscillation, *Mon. Weather Rev.*, *122*, 669–688.
- McPhaden, M. J., X. Zhang, H. H. Hendon, and M. C. Wheeler (2006), Large scale dynamics and MJO forcing of ENSO variability, *Geophys. Res. Lett.*, *33*, L16702, doi:10.1029/2006GL026786.
- Muñoz, R., and R. Garreaud (2005), Dynamics of the low-level jet off the subtropical west coast of South America, *Mon. Weather Rev.*, *133*, 3661–3677, doi:10.1175/MWR3074.1.
- Ramos, M., B. Dewitte, O. Pizarro, and G. Garric (2008), Vertical propagation of the extra-tropical Rossby wave during the 1997–1998 El Niño off the west coast of South America in a medium-resolution OGCM simulation, *J. Geophys. Res.*, *113*, C08041, doi:10.1029/2007JC004681.
- Renault, L., B. Dewitte, M. Falvey, R. Garreaud, V. Echevin, and F. Bonjean (2009), Impact of atmospheric coastal jets on SST off central Chile from satellite observations (2000–2007), *J. Geophys. Res.*, *114*, C08006, doi:10.1029/2008JC005083.
- Roundy, P. E., and G. N. Kiladis (2006), Observed relationship between oceanic Kelvin waves and atmospheric forcing, *J. Clim.*, *19*, 5253–5272, doi:10.1175/JCLI3893.1.
- Smith, R. L. (1978), Poleward propagating perturbations in currents and sea levels along the Peru coast, *J. Geophys. Res.*, *83*, 6083–6092, doi:10.1029/JC083iC12p06083.
- Spiegel, M. R. (1990), *Schaum's Outline of Theory and Problems of Statistics*, 504 pp., McGraw-Hill, New York.
- Stuart, D. W. (1981), Sea-surface temperatures and winds during JOINT II: 2. Temporal fluctuations, in *Coastal Upwelling, Coastal Estuarine Sci. Ser.*, vol. 1, edited by F. A. Richards, pp. 32–38, AGU, Washington, D. C.
- Torrence, C., and G. P. Compo (1998), A practical guide to wavelet analysis, *Bull. Am. Meteorol. Soc.*, *79*, 61–78, doi:10.1175/1520-0477(1998)079<0061:APGTWA>2.0.CO;2.
- Vecchi, G. A., and N. A. Bond (2004), The Madden–Julian Oscillation (MJO) and northern high latitude wintertime surface air temperatures, *Geophys. Res. Lett.*, *31*, L04104, doi:10.1029/2003GL018645.
- Wallace, J. M., C. Smith, and C. S. Bretherton (1992), Singular value decomposition of wintertime sea surface temperature and 500-mb height anomalies, *J. Clim.*, *5*, 561–576, doi:10.1175/1520-0442(1992)005<0561:SVDOWS>2.0.CO;2.
- Wentz, F. J., C. Gentemann, D. Smith, and D. Chelton (2000), Satellite measurements of sea surface temperature through clouds, *Science*, *288*, 847–850, doi:10.1126/science.288.5467.847.
- Wheeler, M., and H. Hendon (2004), An all-season real-time multivariate MJO index: Development of an index for monitoring and prediction, *Mon. Weather Rev.*, *132*, 1917–1932, doi:10.1175/1520-0493(2004)132<1917:AARMMI>2.0.CO;2.
- Wheeler, M. C., and G. N. Kiladis (1999), Convectively coupled equatorial waves: Analysis of clouds and temperature in the wavenumber–frequency domain, *J. Atmos. Sci.*, *56*, 374–399, doi:10.1175/1520-0469(1999)056<0374:CCEWAO>2.0.CO;2.
- Yasunari, T. (1981), Structure of an Indian summer monsoon system with a period around 40 days, *J. Meteorol. Soc. Jpn.*, *59*, 336–354.
- Yeh, S.-W., S.-J. Kug, B. Dewitte, M.-H. Kwon, B. P. Kirtman, and F.-F. Jin (2009), El Niño in a changing climate, *Nature*, *461*, 511–514, doi:10.1038/nature08316.

B. Dewitte, K. Goubanova, and S. Illig, Laboratoire d'Etudes en Géophysique et Océanographie Spatiale, 14 Ave. Edouard Belin, F-31400 Toulouse, France. (bxd@legos.obs-mip.fr)

D. Gushchina, Faculty of Geography, Moscow State University, GSP-1, 1 Leninskiye Gory, 119991 Moscow, Russia.

K. Mosquera and K. Takahashi, Instituto Geofísico del Perú, Calle Badajoz 169, Urb Mayorazgo IV Etapa, Ate Vitarte, Lima 03, Perú.

S. Purca, Instituto del Mar del Perú, Esquina Gamarra y General Valle S/N, Chucuito, Callao 22, Perú.

L. Renault, Mediterranean Institute for Advanced Studies, C/Miquel Marques 21, Balearic Islands, E-07190 Esporles, Spain.